Research Article

Journal of Environmental Nanotechnology

Green-synthesized $MnFe_2O_4$ Magnetic Nanoparticles for High-performance Tunnel Magnetoresistance-based Biosensing

A. John Pradeep Ebenezer[1], Deepak Sharma[2], Giri, Raghavendran[3*], Pankaj H. Chandankhede[4], L. Ramesh[5] and R. B. R. Prakash[6]

[1]Department of Computer Applications, St. Joseph's College of Arts and Science (Autonomous), Cuddalore, TN, India
[2]Department of Electronics and Communication Engineering, Jaypee University of Engineering and Technology, Guna, MP, India
[3]Department of Robotics and Automation, Rajalakshmi Engineering College, Chennai, TN, India
[4]Department of Electronics and Telecommunication Engineering, G H Raisoni College of Engineering, Nagpur, MH, India
[5]Department of Electronics and Communication Engineering, M. Kumarasamy College of Engineering, Karur, TN, India
[6]Department of Electrical and Electronics Engineering, Koneru Lakshmaiah Education Foundation, Guntur, AP, India
Received: 03.07.2026 Accepted: 01.08.2026 Published: xx.xx.xxxx
*girir45248@gmail.com

ABSTRACT

The tunnel magnetoresistance (TMR)-based biosensing platform was developed and evaluated using $MnFe_2O_4$ magnetic nanoparticles synthesized through both a conventional co-precipitation route and a green synthesis approach employing *Cucurbita moschata* leaf extract. The sensing system incorporated a commercial TMR2905 sensor coupled with differential operational amplifier to enhance the sensor output voltage. The amplified analog signal was changed into high-resolution digital signal by 16-bit ADS1115 AD converter, while an Arduino Uno microcontroller acquired digital data through I^2C interface and transmitted the sensing response to a computer for real-time monitoring. Magnetic characterization confirmed the soft-ferromagnetic nature of the synthesized nanoparticles, exhibiting saturation magnetization of 61.50 emu/g for conventionally synthesized (CS)-$MnFe_2O_4$, 66.80 emu/g for green synthesized (GS)-$MnFe_2O_4$ (1:9), and 34.20 emu/g for GS-$MnFe_2O_4$ (2:8). Variations in magnetic behavior directly influenced the sensing characteristics of the developed biosensor. The proposed TMR platform achieved a rapid response time of 30 s and delivered sensitivity of 4.90, 4.20, and 4.00 mV/(mg/mL), with corresponding detection limits of 1.20, 1.05, and 1.30 mg/mL for CS-$MnFe_2O_4$, GS-$MnFe_2O_4$ (1:9), and GS-$MnFe_2O_4$ (2:8), respectively. Among the investigated formulations, the green synthesized-$MnFe_2O_4$ (1:9) sample exhibited the highest sensing efficiency owing to its superior magnetic performance, whereas the GS-$MnFe_2O_4$ (2:8) formulation offered an attractive compromise between sensing capability and environmentally sustainable synthesis. The developed TMR sensing platform integrated with green-derived $MnFe_2O_4$ magnetic nanolabels demonstrates considerable potential for rapid, highly sensitive, and sustainable biosensing applications.

Keywords: Magnetoresistance; Green synthesis; Analog signal; Biosensor; Magnetic performance.

1. INTRODUCTION

The growing demand for rapid, reliable, and miniaturized sensing systems has accelerated the development of magnetic biosensors for biomedical analysis, environmental surveillance, food quality assessment, and portable diagnostic applications. In comparison with conventional laboratory-based analytical techniques, magnetic biosensors provide rapid response, simplified sample handling, high measurement stability, and compatibility with compact electronic platforms. Recent progress in tunnel magnetoresistance (TMR) sensing technology, magnetic nanomaterials, low-noise signal conditioning circuits, and embedded data acquisition systems has significantly improved the sensitivity and practical applicability of these devices. In particular, the integration of functional magnetic nanoparticles with TMR sensors enables efficient magnetic signal transduction while eliminating complex optical detection components. Green-synthesized $MnFe_2O_4$ nanoparticles derived from *Cucurbita moschata* leaf extract offer an environmentally benign alternative to conventional synthesis (CS) routes, providing suitable magnetic characteristics for biosensing applications. When coupled with a high-resolution TMR sensing platform, these magnetic nanolabels facilitate rapid and sensitive magnetic signal detection, highlighting their potential for next-generation portable biosensing systems and point-of-care diagnostic technologies (Sayad *et al.* 2022). Similarly, a microfluidic biochip integrated with a microcontroller and a TCS3200 color sensor successfully performed automated blood calcium detection using small sample volumes while maintaining good agreement with conventional spectroscopic methods (Al-Sawaff *et al.* 2022). A wireless cyber-physical digital microfluidic

biochip further improved portable biochemical analysis by integrating microcontrollers, mobile communication modules, and secure encryption algorithms for reliable data transmission (Yao *et al.* 2023).

The accuracy and reliability of biosensing platforms have also been enhanced through automation and intelligent instrumentation. A fully automatic biochip spotting system based on an STM32 microcontroller improved spotting precision through the integration of closed-loop displacement sensors, stepper motors, and OLED monitoring, enabling highly reproducible biochip fabrication (Li *et al.* 2020). Likewise, an automated surface plasmon resonance sensing platform incorporating motors, distance sensors, temperature sensors, and touchscreen control achieved accurate optical alignment and highly repeatable sensing performance comparable with manually adjusted systems (Da Silva *et al.* 2021). The integration of embedded electronics enhances biosensor precision and reliability, while magnetoresistive biosensors and magnetic nanoparticles enable sensitive, interference-free detection. Giant magnetoresistance (GMR) biosensors have demonstrated remarkable analytical performance in recent years. Spin-valve GMR thin-film biosensors configured using half- and quarter-Wheatstone bridge circuits achieved highly sensitive biomolecule detection when coupled with green-synthesized Fe_3O_4@Ag magnetic labels, with the half-bridge configuration providing superior sensitivity and measurement stability (Garcia *et al.* 2023). Furthermore, dual-chip GMR employing green-synthesized Fe_3O_4/PEG magnetic nanoparticles demonstrated higher analytical sensitivity than the corresponding single-chip configuration for α-amylase detection, confirming the advantages of differential sensing architectures (Ardiyanti *et al.* 2025).

Tunnel magnetoresistance technology has recently attracted considerable attention, because of its higher magnetoresistance ratio and superior magnetic field sensitivity compared with conventional GMR sensors. The TMR-based biosensor with green-synthesized Fe_3O_4/Ag magnetic nanoparticles successfully detected albumin by both single-chip and dual-chip configurations, where the dual-chip arrangement achieved a sensitivity of 29.75 mV/(mg/mL), detection below 1 mg/mL, and stable measurements within 30 s (Swastika *et al.* 2025). Real-time of FeCrNbB magnetic nanoparticles embedded in epoxy resin was also successfully demonstrated using a TMR sensor with magnetoresistance of approximately 53% and sensitivity 1.24 %/Oe, highlighting its potential for magnetic hyperthermia and cancer localization (Ghemes *et al.* 2023). Moreover, a low-cost magnetic tunnel junction (MTJ)-based TMR sensor was developed for detecting airborne manganese ferrite nanoparticles in PM2.5, demonstrating excellent portability and environmental monitoring capability (Amara *et al.* 2023). A highly sensitive MTJ sensor employing a synthetic antiferromagnetic free layer further detected magnetic nanoparticle concentrations below 0.01 mg/mL, illustrating the outstanding sensitivity achievable with advanced TMR sensor architectures (Jin *et al.* 2021). Ferrite nanoparticles are promising magnetic labels for magnetoresistive biosensors because of their excellent stability, biocompatibility, tunable magnetic properties, and surface functionalization capability. Superparamagnetic $MnFe_2O_4$ nanoparticles functionalized with citric acid have been successfully employed as magnetic labels for lateral flow immunoassays, exhibiting higher inductive detection sensitivity than conventional Fe_3O_4 nanoparticles for quantitative biomarker detection (Pilati *et al.* 2024). Likewise, polycrystalline Fe_3O_4 and $MnFe_2O_4$ nanoparticles synthesized through the auto-combustion method exhibited enhanced saturation magnetization, superparamagnetic behaviour, and excellent potential for biomedical drug delivery applications (Dhillon *et al.* 2020).

Recent investigations have demonstrated that the magnetic behaviour of ferrite nanoparticles can be effectively tailored through compositional engineering and synthesis optimization. Hydrothermally synthesized Ni-doped CuO nanoparticles exhibited enhanced magnetic moments at an optimum Ni concentration, confirming that controlled elemental substitution can significantly influence magnetic performance (Chandrasekar *et al.* 2022). Similarly, Cd incorporation into TiO_2 nanoparticles modified their structural, optical, magnetic, and photocatalytic properties, indicating that dopant engineering is an effective strategy for tuning multifunctional nanomaterials (Chandrasekar *et al.* 2023). Green-synthesized Fe_3O_4 nanoparticles prepared using *Moringa oleifera* extract also demonstrated reduced crystallite size, balanced phase purity, and high saturation magnetization, illustrating the capability of plant-mediated synthesis to produce magnetic nanoparticles with excellent structural and magnetic characteristics (Tabrani *et al.* 2025).

Green synthesis has emerged alternative to conventional methods, utilizing plant-derived phytochemicals as natural reducing, capping, and stabilizing agents to minimize hazardous chemicals and enhance nanoparticle biocompatibility. Green-synthesized silicon nanoparticles prepared using *Ocimum basilicum purpurascens* extract were successfully employed as non-enzymatic glucose biosensors, exhibiting excellent photoluminescence response, high sensitivity, and improved stability for glucose monitoring (Montoya-Leyva *et al.* 2025). Furthermore, advanced optical, electrochemical, and biosensing nanosensors have been highlighted as promising tools for monitoring nanoparticle transport, accumulation, and physiological responses in plants, demonstrating the growing importance of intelligent nanosensors in precision

agriculture and environmental monitoring (Parimalagandhi *et al.* 2025).

Plant-derived biomolecules have also attracted attention beyond biosensing because of their multifunctional physicochemical properties. Biogenic SiO_2 nanoparticles derived from diatomaceous biosludge and functionalized with APTES significantly enhanced thermal stability, infrared emissivity, solar reflectance, and mechanical strength when incorporated into geopolymer radiative cooling coatings (Gayathri *et al.* 2026). Likewise, *Cucurbita moschata* leaf extract incorporated into poly(ε-caprolactone)/polylactic acid composites enhanced antimicrobial activity against various pathogens while demonstrating the biological activity of phytochemical constituents present in the plant extract (Pekdemir *et al.* 2022). These studies collectively demonstrate that plant-mediated synthesis offers a sustainable pathway for producing functional nanomaterials with improved physicochemical and biological properties. Besides nanomaterial development, significant progress has also been achieved in magnetic sensing materials and intelligent sensing systems. Electrodeposited Co–Ni–P/Zn multilayer coatings exhibited pronounced magnetic field-dependent magnetoimpedance behaviour, confirming their suitability for magnetic sensing applications (Kanthiah *et al.* 2026).

Simultaneous characterization of magnetic properties and temperature during current annealing has also been realized through microscope-based measurement platforms capable of monitoring crystallization and microstructural evolution in real time (Moron-Fernandez *et al.* 2021). Moreover, self-sustaining IoT sensing systems integrating perovskite photovoltaics, carbon electrodes, and supercapacitors have enabled battery-free autonomous sensing for temperature and strain monitoring, illustrating the future direction of intelligent sensing technologies (Shanavash *et al.* 2026).

Although significant progress has been achieved in magnetic biosensor technology, the development of environmentally sustainable sensing platforms based on green-synthesized magnetic nanomaterials remains relatively unexplored. Most existing investigations have primarily focused on chemically synthesized ferrite nanoparticles or conventional Fe_3O_4 magnetic labels, whereas comprehensive studies examining the influence of plant-mediated synthesis conditions on the physicochemical, magnetic, and sensing characteristics of $MnFe_2O_4$ nanoparticles are still very limited. In the present work, a TMR-based biosensing system was designed using $MnFe_2O_4$ synthesized through both conventional and *Cucurbita moschata* (CM) leaf extract-assisted green synthesis. The effect of varying CM leaf extract-to-NH_4OH ratios on phase formation, microstructure, surface functionalization, and magnetic properties was systematically evaluated to understand their influence on biosensor performance. The synthesized nanoparticles were characterized by X-ray diffraction (XRD), Fourier transform infrared spectroscopy (FTIR), scanning electron microscopy (SEM), and vibrating sample magnetometry (VSM). Their applicability as magnetic labels was subsequently assessed using a TMR2905 sensor integrated by differential operational amplifier, 16-bit ADS1115 AD converter, and an Arduino Uno-based data acquisition system. The correlations between the structural and magnetic characteristics of the $MnFe_2O_4$ nanoparticles and the corresponding TMR sensing responses were established to determine the optimum synthesis condition for achieving rapid, highly sensitive, and environmentally sustainable magnetic biosensing.

2. MATERIALS AND METHODS

2.1 Materials

Fresh *Cucurbita moschata* leaf extract was used for the green synthesis of $MnFe_2O_4$ nanoparticles. It was procured from Sai Laboratory, Coimbatore, India. Ferric chloride hexahydrate ($FeCl_3{\cdot}6H_2O$, 99% purity), manganese chloride tetrahydrate ($MnCl_2{\cdot}4H_2O$, 99% purity), and ammonium hydroxide (NH_4OH) were employed as precursors and precipitating reagents and were obtained from Star Scientific Solutions, Erode, India. Deionized (or distilled) water served as the solvent for all synthesis and washing procedures. All reagents were of analytical grade and were utilized directly without any additional purification or pretreatment.

2.2 Preparation of Sample

2.2.1 CM Extract Preparation

The *Cucurbita moschata* leaf extract was prepared by dispersing the collected extract material in distilled water, followed by continuous magnetic stirring at 60 °C for 1 hour. As illustrated in Fig. 1(a), this process produced homogeneous green solution, indicating the successful extraction of bioactive phytochemical constituents for the subsequent green synthesis of $MnFe_2O_4$ nanoparticles (Lambertini *et al.* 2021). After naturally cooling to ambient temperature, the prepared extract was filtered through Whatman filter paper, and the clear filtrate was refrigerated until further use in the synthesis process.

2.2.2 Preparation of $MnFe_2O_4$ NPs

A precursor solution were prepared by adding 1.484 g of $MnCl_2{\cdot}4H_2O$ and 4.054 g of $FeCl_3{\cdot}6H_2O$ in distilled water with continuous stirring while maintaining a Mn^{2+}:Fe^{3+} molar ratio of 1:2 to synthesize $MnFe_2O_4$ nanoparticles (Swastika *et al.* 2024). Different *Cucurbita*

moschata leaf extract:10% NH_4OH volume ratios were employed to prepare green-synthesized $MnFe_2O_4$ nanoparticles, depicted in Fig. 1(b,c). The reaction suspension was continuously stirred at 600 rpm for 90 minutes, where alkaline medium induced nanoparticle precipitation and the CM phytochemicals facilitated particle formation and stabilization. The resulting precipitate was washed several times with deionized water until a neutral pH (~7) was attained, magnetically separated, and subsequently dried in a hot-air oven at 100 °C for 2 hours. Table 1 shows the synthesis parameters for CS-synthesized and GS-synthesized $MnFe_2O_4$ (at different concentrations).

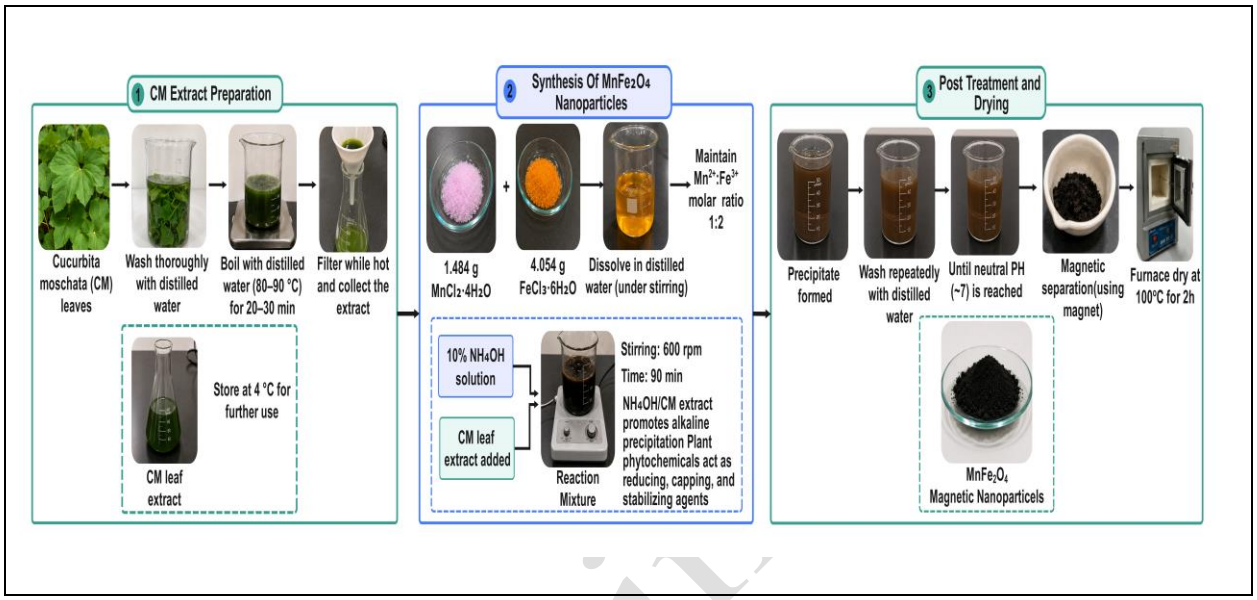

Fig. 1: $MnFe_2O_4$ synthesis methodology

Table 1. Synthesis parameters of $MnFe_2O_4$

Material	CM Extract	10% NH_4OH	Total Alkaline Volume	CM Fraction	CM: NH_4OH
CS-$MnFe_2O_4$	0	45	45	0	0 : 10
GS-$MnFe_2O_4$	4.5	40.5	45	10	1 : 9
GS-$MnFe_2O_4$	9.0	36.0	45	20	2 : 8
GS-$MnFe_2O_4$	13.5	31.5	45	30	3 : 7
GS-$MnFe_2O_4$	18.0	27.0	45	40	4 : 6

2.3 Characterization

The structural and morphological characteristics of the synthesized $MnFe_2O_4$ nanoparticles were examined. Phase identification and crystallographic analysis were performed using X-ray diffraction (XRD) on a Bruker D8 Advance diffractometer equipped with Cu-Kα radiation (λ = 1.5406 Å) (Yadav *et al.* 2020). Surface morphology, elemental composition, and elemental distribution were characterized by scanning electron microscopy integrated with EDX on a Zeiss Gemini instrument. The magnetic behavior of synthesized $MnFe_2O_4$ nanoparticles was evaluated by Oxford 1.2 H vibrating sample magnetometer. The surface functional groups were identified by Fourier transform infrared spectroscopy using a Shimadzu spectrometer (Nawale *et al.* 2026).

2.4 Experimental Measurement Setup

As shown in Fig. 2, the sensing system comprised a Helmholtz coil and a TMR2905 tunnel magnetoresistance sensor integrated with custom-built circuit. Constant current of 0.33 A were applied to Helmholtz coil to generate magnetic field of 4 Oe, thereby optimizing sensor response. This operating field was selected because TMR2905 provides maximum sensitivity within 4–5 Oe magnetic field range (Rizki *et al.* 2026). A constant 4 Oe magnetic field was maintained for 30 s at each measurement ensuring consistent sensing conditions.

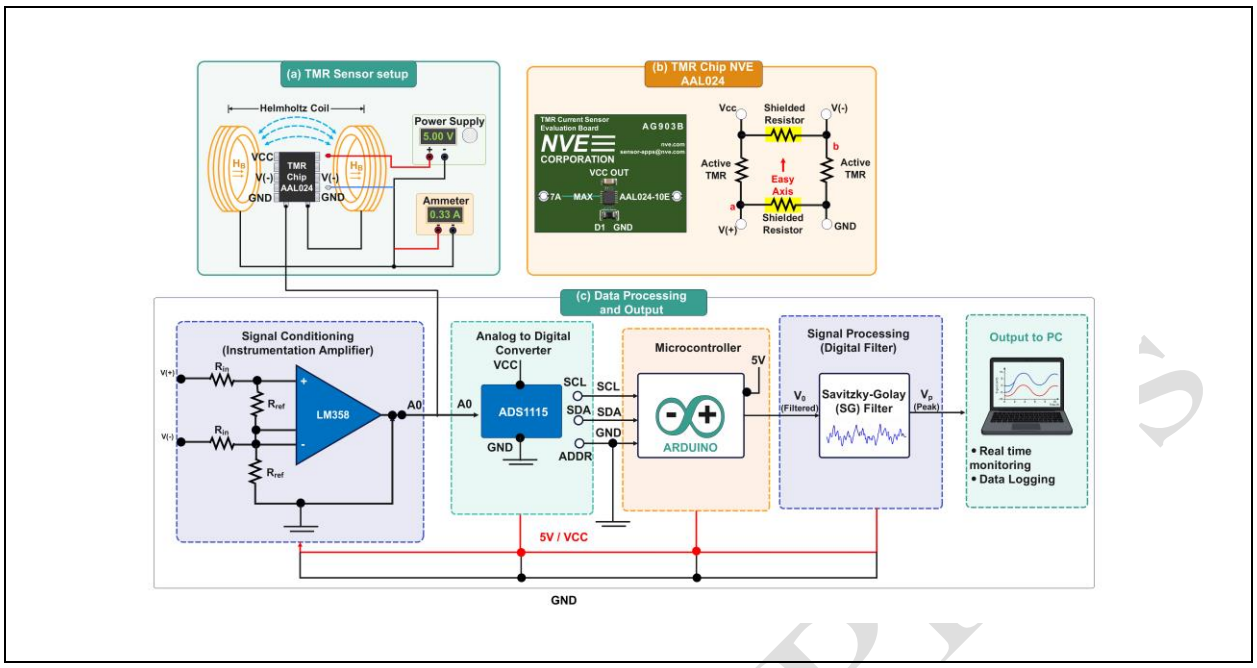

Fig. 2: (a) Sensor testing setup, (b) TMR chip and (c) Measurement acquisition system

Two analog output signals generated by the TMR2905 sensor were processed using an LM358-based differential operational amplifier to enhance the voltage response. To improve measurement accuracy, precision resistors with values of 2.2 ± 0.1 MΩ (R_{ref}) and 100 ± 1 kΩ (R_{in}) were incorporated into the amplifier circuit. The conditioned output voltage was digitized using 16-bit ADS1115 analog-to-digital converter, and the digital data were acquired by an Arduino Uno through the I^2C communication interface. This configuration eliminates the limitations of the Arduino's built-in 10-bit ADC, enabling reliable detection of small voltage variations generated by the TMR sensor. The Arduino Uno simultaneously supplied a regulated 5 V input to the sensing circuit. To suppress measurement noise while preserving the signal profile, the acquired data were smoothed using a local polynomial least-squares fitting filter. This approach enhanced the signal-to-noise ratio without altering the characteristic peak features, resulting in stable and accurate magnetic signal detection from the synthesized $MnFe_2O_4$ nanoparticle labels (Wang *et al.* 2020). The SG-filtered output (V_p) yielded a stable and accurate representation of the magnetic response produced by the $MnFe_2O_4$ nanoparticle labels.

2.5 Alcohol-based Nanoparticle Dispersion

For each $MnFe_2O_4$ nanoparticle sample, ethanol suspensions with concentrations of 5, 15, 25, 35, and 45 mg/mL were prepared to investigate the concentration-dependent TMR sensor response. The required nanoparticle mass was dispersed in fixed volume of ethanol to ensure uniform sample preparation. Each suspension was deposited onto the sensing region and allowed dry naturally for 1 minute. After solvent evaporation, SG-filtered output voltage (V_p) was measured during three successive 30 s cycles (Tests 1–3) for every concentration. Throughout the measurements, a constant magnetic bias field of 4 Oe was maintained to ensure reproducible sensing conditions.

2.6 TMR Sensing Methodology

For each measurement, approximately 2 µL of the ethanol-dispersed $MnFe_2O_4$ nanoparticle suspension was deposited onto the active area of the TMR2905 sensor using a calibrated micropipette. The selected volume ensured complete coverage of the sensing region without contacting the surrounding electrodes. After each experiment, the sensor surface was gently cleaned with ethanol using a cotton swab to remove residual nanoparticles. Since the initial baseline was not completely restored after cleaning, a fresh baseline voltage was acquired before every measurement to ensure reliable comparison of the sensor responses.

3. RESULTS AND DISCUSSION

$MnFe_2O_4$ nanoparticles were prepared by a plant-assisted co-precipitation route using ferric chloride hexahydrate ($FeCl_3 \cdot 6H_2O$) and manganese chloride tetrahydrate ($MnCl_2 \cdot 4H_2O$) as the Mn^{2+} and Fe^{3+} sources, respectively. The proposed formation pathway, illustrated in Fig. 3, involves three sequential steps. During the initial nucleation stage, phytochemicals present in the CM leaf extract, such as flavonoids and phenolic compounds, coordinate with the metal ions through hydroxyl- and carbonyl-containing functional groups.

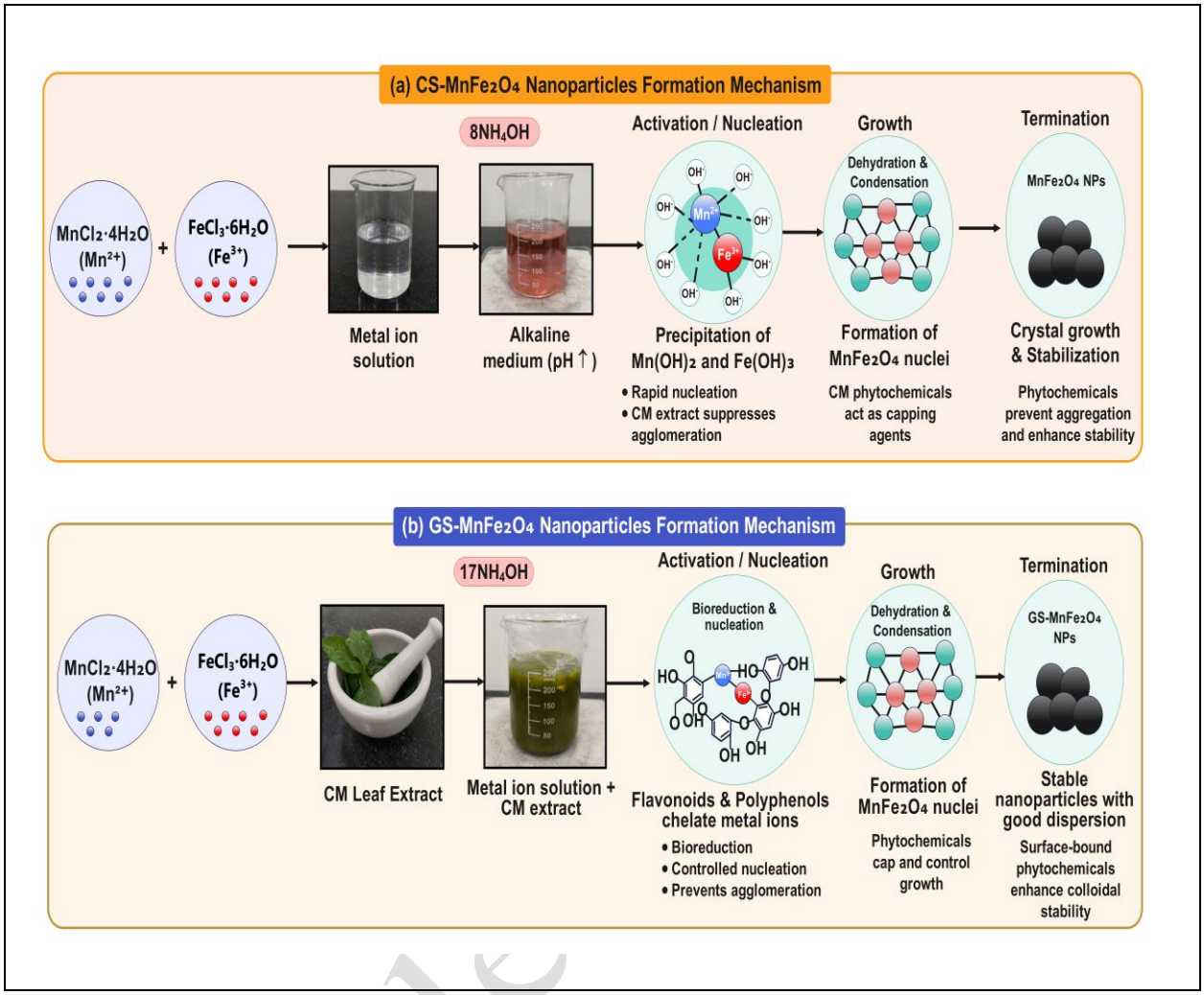

Fig. 3: $MnFe_2O_4$ formation mechanism: (a) CS-$MnFe_2O_4$ and (b) GS- $MnFe_2O_4$

NH_4OH provides the alkaline environment required for the precipitation of manganese and iron hydroxides, while the plant extract regulates nucleation and limits particle agglomeration. In the crystal growth stage, the hydroxide precursors undergo condensation and dehydration to generate the spinel $MnFe_2O_4$ phase. The adsorbed biomolecules simultaneously act as natural surface-capping agents, restricting crystal growth and improving particle dispersion. During the final stabilization stage, continued crystallization enhances structural integrity, whereas the surface-bound phytochemicals inhibit aggregation and improve nanoparticle stability. Consequently, the green co-precipitation approach combines efficient alkaline precipitation with the stabilizing action of naturally derived biomolecules, enabling the controlled synthesis of $MnFe_2O_4$ nanoparticles. The chemical reactions corresponding to the conventional and green-assisted synthesis routes are summarized in Eqs. (1) and (2), respectively (Nemčeková *et al.* 2025).

Step 1. Formation of $MnFe_2O_4$ nanoparticles.

$$Mn^{2+}_{(aq)} + 2Fe^{3+}_{(aq)} + 8OH^{-}_{(aq)} \rightarrow Mn(OH)_{2(aq)} \ldots (1)$$

Step 2. Green-assisted formation using *Cucurbita moschata* extract

$$CM_{(aq)} + Mn^{2+}_{(aq)} + 2Fe^{3+}_{(aq)} + 8OH^{-}_{(aq)} \rightarrow CM - MnFe_2O_{4(s)\downarrow} \downarrow + 4H_2O_{(l)} \quad \ldots (2)$$

Table 2 provides the different measurements used for $MnFe_2O_4$ suspension preparation.

Table 2. $MnFe_2O_4$ suspension preparation

Concentration (mg/ mL)	Volume of Ethanol (mL)	Mass of $MnFe_2O_4$ (mg)
5	0.5	0.5
15	0.1	1.5
25	0.1	2.5
35	0.1	3.5
45	0.1	4.5

3.1 Structural Phase Characterization

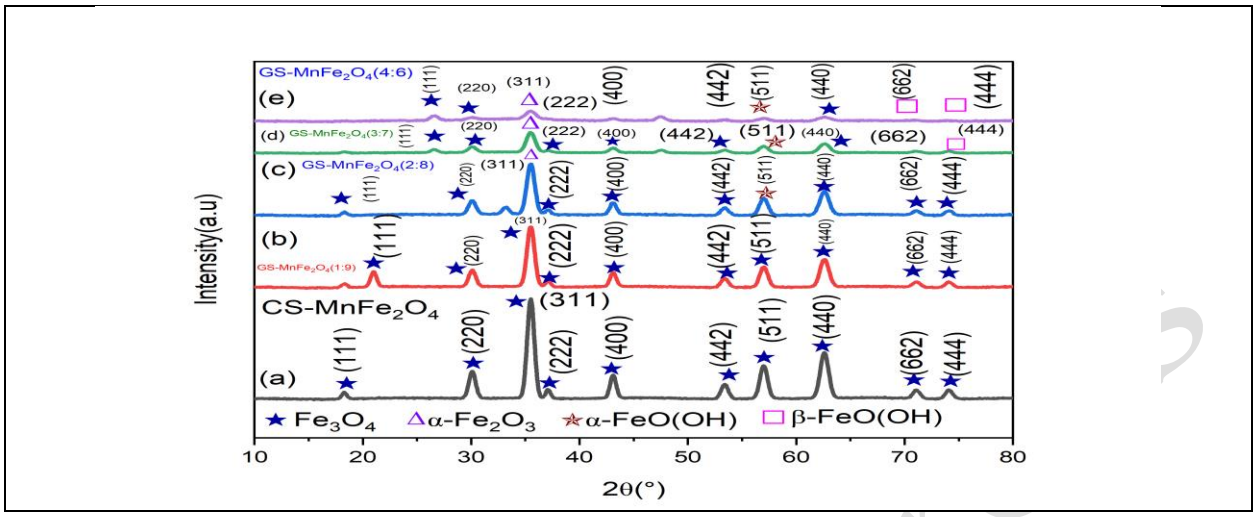

Fig. 4: Xray diffraction of (a) Conventionally synthesized-$MnFe_2O_4$ (b-e) Green-synthesized-$MnFe_2O_4$

X-ray diffraction was employed to examine crystalline phases, crystal structure, and crystallite size of $MnFe_2O_4$ nanoparticles synthesized by green synthesis (GS-$MnFe_2O_4$) and conventional co-precipitation (CS-$MnFe_2O_4$) by CM:NH_4OH ratios of 1:9, 2:8, 3:7, and 4:6. As presented in Fig. 4, all diffraction patterns exhibited the characteristic reflections of cubic spinel $MnFe_2O_4$ at 2θ values of 18.3° (111), 30.1° (220), 35.55° (311), 37.15° (222), 43.1° (400), 53.35° (422), 57.05° (511), 62.65° (440), and 71.15° (622), consistent with the standard reference (COD No. 9006920). Weak diffraction peaks observed at 74.05° (444) were assigned to α-Fe_2O_3, which may have formed through partial oxidation during the drying process (Eq. 3) (Yadav *et al.* 2020).

$$Mn(OH)_{2(aq)} + 2Fe(OH)_{3(aq)} \rightarrow MnFe_2O_{4(s)} \downarrow + 4H_2O_{(l)} \quad \ldots (3)$$

Furthermore, the XRD results indicate that increasing the CM extract content while reducing the NH_4OH proportion influenced phase evolution during $MnFe_2O_4$ synthesis. The CS-$MnFe_2O_4$ sample displayed a weak diffraction peak at 2θ = 21.1° indexed to (111) plane of α-FeO(OH) (goethite). In contrast, the GS-$MnFe_2O_4$ samples prepared with higher CM:NH_4OH ratios (3:7 and 4:6) exhibited additional reflections at 2θ = 26.6° and 26.4°, assigned to the (111) plane of Fe_3O_4 (magnetite). These observations suggest that the CM extract-to-NH_4OH ratio plays an important role in controlling phase formation, where insufficient alkalinity promotes the formation of iron oxyhydroxide by-products. The average crystallite size of each sample were determined using Debye–Scherrer equation (Eq. 4) (Alghamdi *et al.* 2023):

$$D = \frac{k\lambda}{\beta \cos\theta} \quad \ldots (4)$$

The XRD analysis revealed a gradual reduction in the average crystallite size 8.112 nm for CS- $MnFe_2O_4$ to 8.129 nm for GS- $MnFe_2O_4$ (4:6), corresponding to an overall decrease of approximately 52.47% with increasing CM extract content. This refinement in crystallite size is associated with the phytochemical-mediated regulation of crystal growth, reflected by the broadening and reduced intensity of the (311) diffraction peak, together with the appearance of the β-FeO(OH) (akaganeite) phase, which commonly exhibits crystallite sizes of 3–6 nm. To further evaluate the crystal structure, MAUD refinement was performed to determine the crystallite size distribution, lattice parameters, and phase fractions, and the results are presented Tables 3 and 4.

Table 3. Lattice parameters and crystallite size

Sample	Lattice Parameter (Å)	Crystallite Size (nm)
CS-$MnFe_2O_4$	8.112 ± 0.006	9.11 ± 0.18
GS-$MnFe_2O_4$ (1:9)	8.114 ± 0.008	8.06 ± 0.17
GS-$MnFe_2O_4$ (2:8)	8.118 ± 0.010	6.94 ± 0.15
GS-$MnFe_2O_4$ (3:7)	8.123 ± 0.012	5.58 ± 0.13
GS-$MnFe_2O_4$ (4:6)	8.129 ± 0.015	4.33 ± 0.11

Table 4. Phase composition of $MnFe_2O_4$

Sample	Phase Percentage (%)			
	Fe_3O_4	$\alpha - Fe_2O_3$	$\alpha - FeO(OH)$	$\beta - FeO(OH)$
CS-$MnFe_2O_4$	95.18	2.16	1.48	1.18
GS-$MnFe_2O_4$ (1:9)	92.64	2.85	2.18	2.33
GS-$MnFe_2O_4$ (2:8)	88.72	3.94	3.42	3.92

GS-$MnFe_2O_4$ (3:7)	84.31	4.86	5.18	5.65
GS-$MnFe_2O_4$ (4:6)	79.58	6.24	6.91	7.27

A consistent reduction in particle size with increasing CM extract content was observed from both characterization methods, although the XRD-derived crystallite sizes exhibited a relatively lower coefficient of determination (R^2 = 0.56). This behavior indicates that CM extract not only suppresses crystal growth but also influences the structural heterogeneity of the synthesized $MnFe_2O_4$ nanoparticles, resulting in greater variation in the XRD-derived crystallite sizes. Surface morphology of the synthesized samples were further investigated by scanning electron microscopy at 5000× and 2500× magnification. As presented in Fig. 5, CS- $MnFe_2O_4$ and GS-$MnFe_2O_4$ samples were mainly composed of nearly spherical nanoparticles, reflecting uniform nucleation and isotropic crystal growth. Nevertheless, increasing the CM extract proportion produced noticeable particle agglomeration and reduced morphological uniformity, indicating that excess phytochemical species affected particle growth and surface stabilization during synthesis.

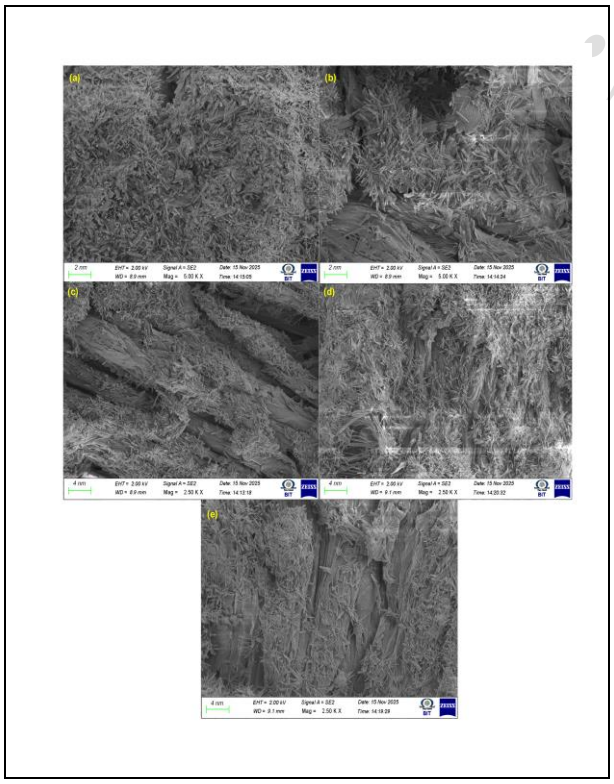

Fig. 5: SEM micrographs of (a) Conventionally synthesized- $MnFe_2O_4$, and Green synthesized- $MnFe_2O_4$ at different ratios: (b) 1:9, (c) 2:8, (d) 3:7, and (e) 4:6

3.2 FTIR Functional Group Analysis

Fourier transform infrared spectra were recorded over 4000–400 cm^{-1} region to identify the chemical bonds and surface functional groups of the CS-$MnFe_2O_4$ NPs and GS-$MnFe_2O_4$ NPs. The spectra verified the formation of manganese ferrite through the characteristic metal–oxygen absorption bands observed in all samples. Typical vibration bands associated with maghemite (612–590 cm^{-1}), hematite (586–574 cm^{-1}) and $MnFe_2O_4$ (584 cm^{-1}), were identified. As shown in Fig. 6(a), CS-$MnFe_2O_4$ displayed a prominent Fe–O stretching vibration at 590-574 cm^{-1}, whereas the GS-$MnFe_2O_4$ (Fig. 6(b–e)) exhibited shifted Fe–O absorption peak 612–574 cm^{-1}, reflecting the influence of CM leaf extract on the crystal lattice. The FTIR spectra also confirmed the incorporation of phytochemical residues on the nanoparticle surface. CS-$MnFe_2O_4$ showed carbonyl (1640-1624 cm^{-1}) and hydroxyl (3430-3410 cm^{-1}) absorption peaks, while the green-synthesized samples exhibited additional aromatic (1390-1378 cm^{-1}) and ether (1110 cm^{-1}) vibrations. Moreover, GS-$MnFe_2O_4$ prepared with higher CM extract contents (3:7 and 4:6) displayed distinct ether-related bands at 1116-1060 cm^{-1}, consistent with the characteristic FTIR spectrum of the CM leaf extract.

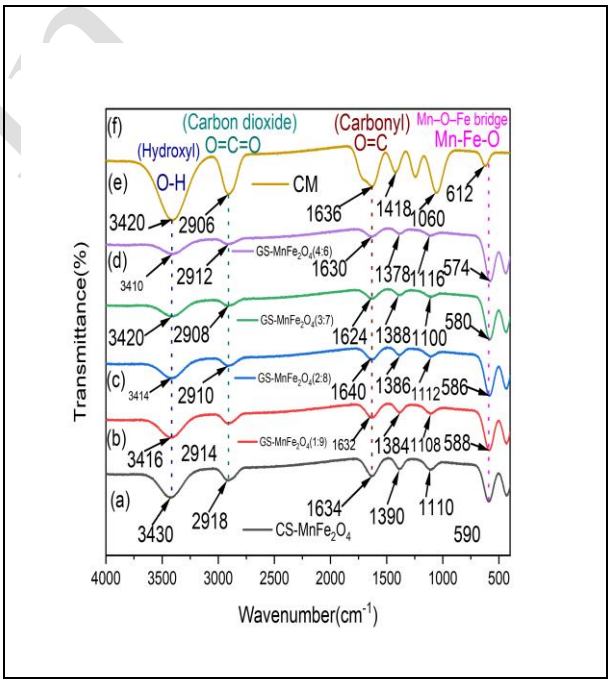

Fig. 6: FTIR spectra of (a) Conventionally synthesized- $MnFe_2O_4$ (b) Green-synthesized- $MnFe_2O_4$ (1:9), (c) Green-synthesized- $MnFe_2O_4$ (2:8), (d) Green-synthesized- $MnFe_2O_4$ (3:7), (e) Green-synthesized - $MnFe_2O_4$ (4:6), and (f) CM

These results indicate that the phytochemical constituents of the CM leaf extract functioned as both reducing and surface-stabilizing agents $MnFe_2O_4$ nanoparticle synthesis, leading to their adsorption on the nanoparticle surface and modification of the surface

chemistry. Although pure CM extract showed aliphatic C–H at 2918-2906 cm^{-1} (Fig. 6(f)), this absorption was not observed at any $MnFe_2O_4$ sample, implying that these functional groups were consumed or chemically transformed during nanoparticle formation. Overall, the FTIR analysis confirms that adjusting the CM extract-to-NH_4 OH ratio systematically modifies the surface functional groups and chemical bonding of $MnFe_2O_4$ NPs.

3.3 Analysis of Magnetic Attributes

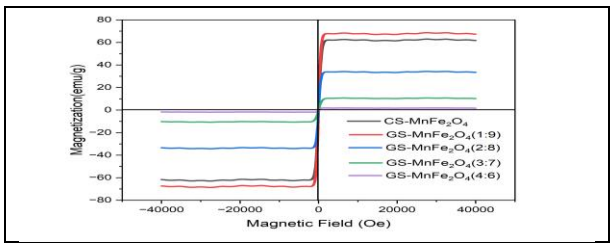

Fig. 7: $MnFe_2O_4$ Hysteresis Curves

The hysteresis curves presented in Fig. 7 for CS-$MnFe_2O_4$ and GS-$MnFe_2O_4$ prepared with CM:NH_4OH ratios of 1:9, 2:8, 3:7, and 4:6 exhibit typical soft-ferromagnetic behavior, including the GS-$MnFe_2O_4$ (4:6) sample, although its loop is comparatively weak. The corresponding magnetic parameters are summarized in Table 5.

The saturation magnetization (M_s) was 61.50 emu/g for CS-$MnFe_2O_4$ and 66.80, 34.20, 10.10, and 1.80 emu/g for GS-$MnFe_2O_4$ synthesized at CM:NH_4OH ratios of 1:9, 2:8, 3:7, and 4:6, respectively. As shown in Fig. 8, the low-field magnetic susceptibility (χ = dM/dH) followed the same trend as the saturation magnetization, indicating that samples with higher M_s exhibited greater magnetic susceptibility. Notably, GS-$MnFe_2O_4$ (1:9) displayed a higher M_s (66.80 emu/g) than CS-$MnFe_2O_4$ (61.50 emu/g), suggesting that optimized CM:NH_4OH ratio (1:9) promoted favorable nucleation and crystal growth, resulting in enhanced magnetic ordering.

Table 5. Magnetic properties of $MnFe_2O_4$

Sample	M_S (emu/g)	M_r (emu/g)	$\chi(\times 10^{-1}$ emu/g.Oe $^{-1})$	H_c (Oe)	$\chi_i(\times 10^{-1}$ emu/g. Oe$^{-1})$	D_s (nm)
CS-$MnFe_2O_4$	61.50	6.76	8.68	71.82	0.82	5.31
GS-$MnFe_2O_4$ (1:9)	66.80	8.09	9.98	82.46	1.16	4.46
GS-$MnFe_2O_4$ (2:8)	34.20	1.84	4.59	29.15	0.40	5.63
GS-$MnFe_2O_4$ (3:7)	10.10	0.26	0.93	27.62	0.04	5.69
GS-$MnFe_2O_4$ (4:6)	1.80	0.22	0.06	7.25	0.01	5.20

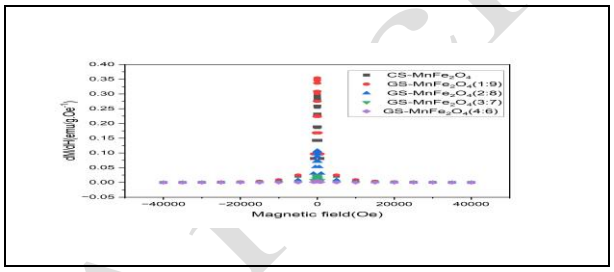

Fig. 8: Switching field distribution analysis

Accordingly, the GS-$MnFe_2O_4$ (1:9) sample exhibited the highest dM/dH value, consistent with its maximum saturation magnetization. This result suggests that an appropriate CM extract-to-NH_4OH ratio can improve the magnetic properties of $MnFe_2O_4$ nanoparticles rather than relying solely on a higher alkaline concentration. The phytochemical constituents of the CM extract likely promoted controlled crystal growth and surface stabilization, thereby enhancing magnetic ordering. In contrast, further increasing the CM extract content in the GS- $MnFe_2O_4$ (2:8), (3:7), and (4:6) samples progressively reduced both the saturation magnetization and magnetic susceptibility. This behavior is attributed to the greater incorporation of non-magnetic organic species and increased surface spin disorder, which weakened the overall magnetic response.

The VSM results showed low coercivity (Hc < 132 Oe) and small remanent magnetization (M_r), confirming that the synthesized $MnFe_2O_4$ nanoparticles possess soft-ferromagnetic characteristics at room temperature despite their nanoscale crystallite size (Ds < 20 nm). This behavior is mainly attributed to magnetic interactions arising from particle agglomeration. Although saturation magnetization predominantly governs the attainable magnetic signal, the coercivity also influences the sensing response under a low magnetic bias field. Because the TMR sensor operates at a bias field of 4 Oe, increased coercivity can restrict complete magnetization of the nanoparticle labels, thereby reducing the generated stray field and the corresponding sensor output. These observations highlight the need to optimize the synthesis conditions to obtain high M_s while minimizing particle aggregation and coercivity for efficient low-field TMR sensing. Furthermore, the magnetic susceptibility (χ) was determined by fitting the experimental magnetization

data using the Langevin model (Eq. 5) to quantitatively describe the field-dependent magnetic behavior (Salama *et al.* 2024).

$$M = M_0 \left[\mathrm{Coth}(\beta\mu H) - \frac{1}{\beta\mu H}\right] \quad \ldots (5)$$

Switching field distribution (SFD) curves shown in Fig. 8 represent magnetic field required for domain reversal in the synthesized $MnFe_2O_4$ nanoparticles. Variations in the SFD peak width among the samples reflect differences in magnetic homogeneity and domain switching behavior. All samples exhibited low initial magnetic susceptibility, consistent with their soft-ferromagnetic nature and nanoscale magnetic domain size (Ds = 4.46–5.63 nm). The magnetic diameter was estimated using Eq. (6) by considering the density of $MnFe_2O_4$ (ρ = 5.18 g/cm^3).

$$D_s = \left[\frac{18k_BT}{\pi\rho M_s^2}\left(\frac{dM}{dH}\right)_{H=0}\right]^{\frac{1}{3}} \quad \ldots (6)$$

Among the prepared $MnFe_2O_4$, the CS-$MnFe_2O_4$, GS-$MnFe_2O_4$ samples synthesized at CM:NH_4OH ratio of 1:9 and 2:8 showed desirable magnetic performance for TMR sensing, owing to their higher low-field magnetic susceptibility (χ = dM/dH), which reflects greater responsiveness under weak magnetic fields. In contrast, the GS-$MnFe_2O_4$ samples with higher CM extract contents (3:7 and 4:6) displayed reduced magnetic sensitivity because the increased phytochemical content weakened the overall magnetic contribution. The results indicate that moderate incorporation of CM extract effectively preserves the magnetic characteristics while retaining the advantages of green synthesis. Therefore, these $MnFe_2O_4$ formulations are well suited for magnetic labels at TMR-based biosensor systems.

3.4 Magnetic Label Detection Performance

Prior to investigating the sensing performance of CS-$MnFe_2O_4$ and GS-$MnFe_2O_4$ (1:9 and 2:8) as magnetic labels, the optimum magnetic bias field (HB) of the TMR2905 sensor was established from its transfer characteristics (Fig. 9). In the absence of magnetic nanoparticles, the TMR sensor displayed a characteristic quasi-step transfer response under the applied magnetic field (Wibowo *et al.* 2024). Average output voltage (VP-avg) increased linearly with applied magnetic field over 2–10 Oe range.

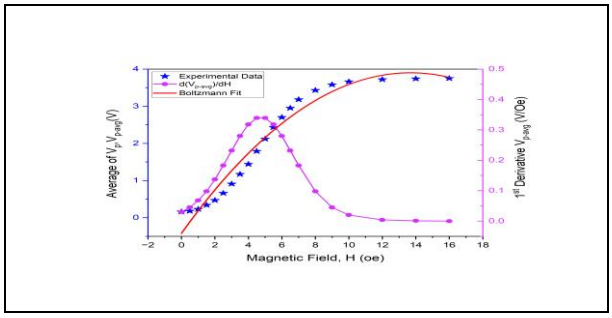

Fig. 9: Bare TMR transfer characteristics

Based on the transfer curve analysis, magnetic bias field of 4 Oe was employed for all subsequent TMR measurements, as it provided the highest sensing response with stable operating conditions. The sensing characteristics, including linearity, repeatability, limit of detection (LoD), and sensitivity were evaluated by conventionally synthesized- $MnFe_2O_4$ and green synthesized-$MnFe_2O_4$ (1:9, 2:8) magnetic labels because the samples exhibited superior magnetic performance compared with the 3:7 and 4:6 formulations. Ethanol suspensions containing 5, 15, 25, 35, and 45 mg/mL of each nanoparticle sample were measured under a constant magnetic bias of 4 Oe, with three consecutive 30 s measurements performed at every concentration. As illustrated in Fig. 10(a–c), Vp-chip represents the baseline output voltage of the bare TMR2905 sensor, whereas Vp corresponds to the output after applying the $MnFe_2O_4$ nanoparticle suspension. The voltage difference (ΔV) between these signals was used to evaluate the sensing response. The corresponding output voltages before and after Savitzky–Golay (SG) filtering are presented in Fig. 11(a–f). To verify measurement repeatability, each concentration was analyzed in three successive tests (Tests 1–3), enabling the influence of signal drift and relaxation effects to be assessed. The TMR sensor produced stable and reproducible responses for all nanoparticle samples, including GS- $MnFe_2O_4$ (2:8), despite its lower magnetic properties than the CS-$MnFe_2O_4$ sample.

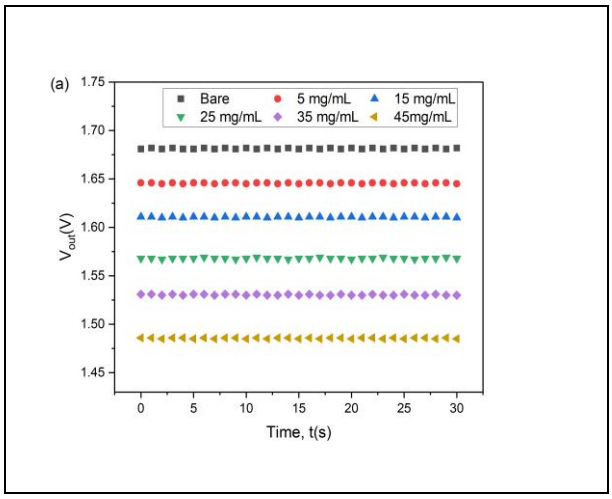

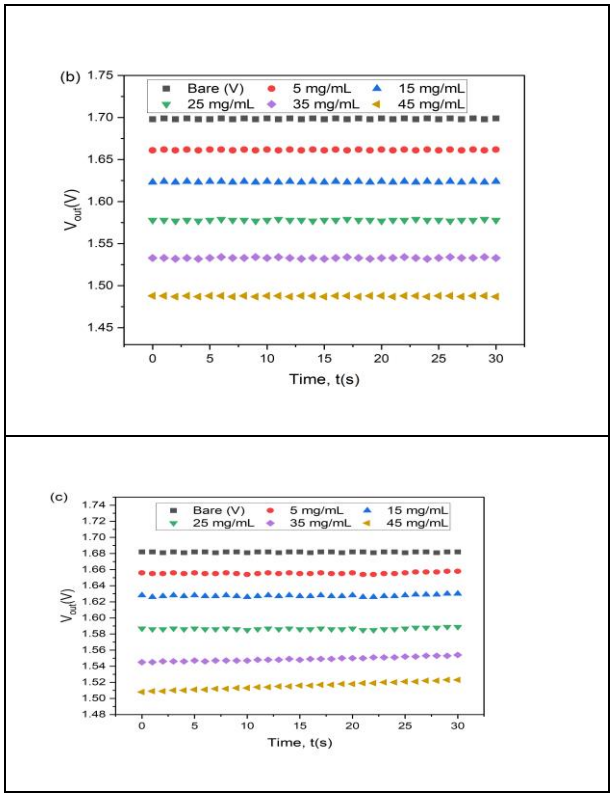

Fig. 10: Output voltage of: (a) CS-$MnFe_2O_4$, (b) GS-$MnFe_2O_4$ (1:9), and (c) GS-$MnFe_2O_4$ (2:8)

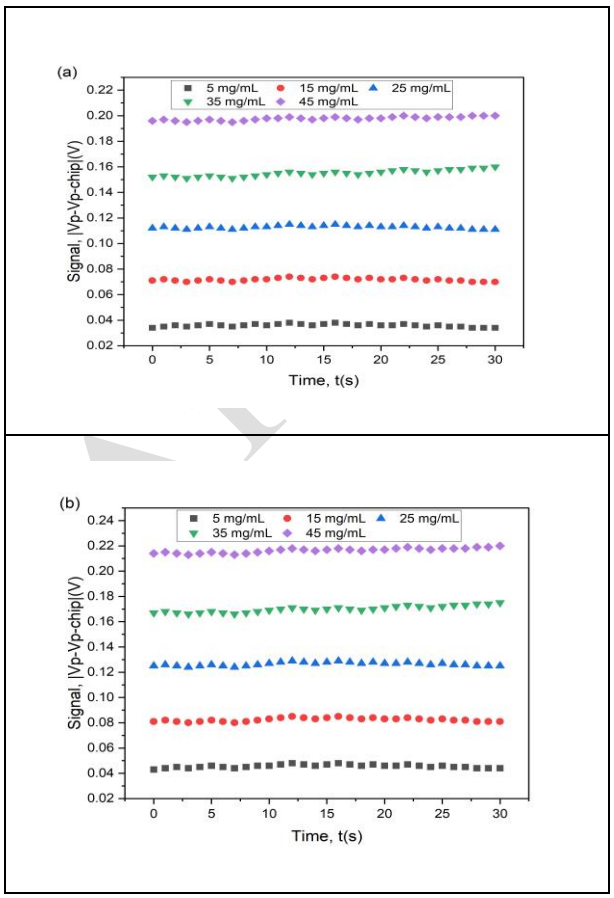

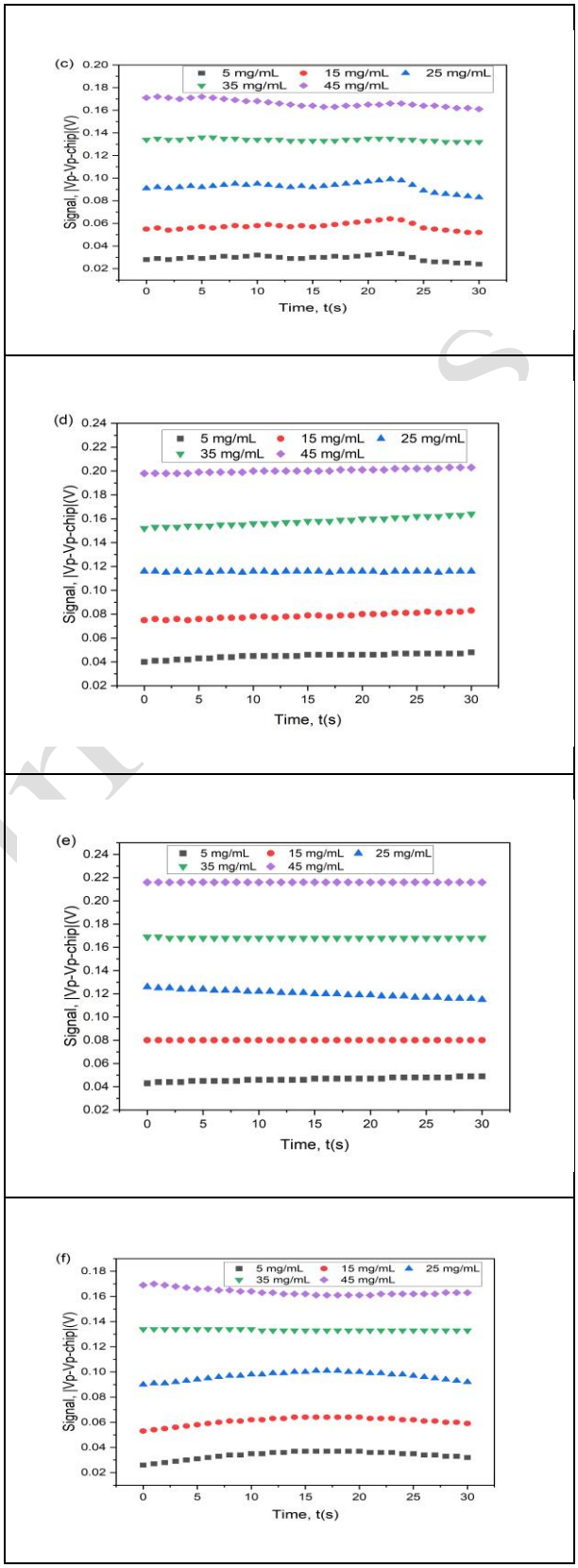

Fig. 11. Sensor repeatability of: (a) CS-$MnFe_2O_4$, (b) GS-$MnFe_2O_4$ (1:9), (c) GS- $MnFe_2O_4$ (2:8) before SG-processed, and (d) CS-$MnFe_2O_4$, (e) GS- $MnFe_2O_4$ (1:9) and (f) GS-$MnFe_2O_4$ (2:8) after SG-processed

As presented in Fig. 12(a), TMR sensor exhibited an excellent linear response over the investigated $MnFe_2O_4$ concentrations, yielding high coefficients of determination (R^2). The calculated sensitivities were 4.90, 4.20, and 4.00 mV/(mg/mL), while the corresponding LoDs were 1.20, 1.05, and 1.30 mg/mL for CS- $MnFe_2O_4$, GS-$MnFe_2O_4$ (1:9), GS-$MnFe_2O_4$ (2:8), respectively. The magnetization measured at the operating bias field of 4 Oe (Mbias) gradually decreased from 7.20 to 6.65 and 3.45 emu/g for the three samples. At concentrations approaching 1 mg/mL, the responses of CS-$MnFe_2O_4$ and GS-$MnFe_2O_4$ (1:9) became nearly identical, indicating that the sensor output was approaching its practical detection limit.

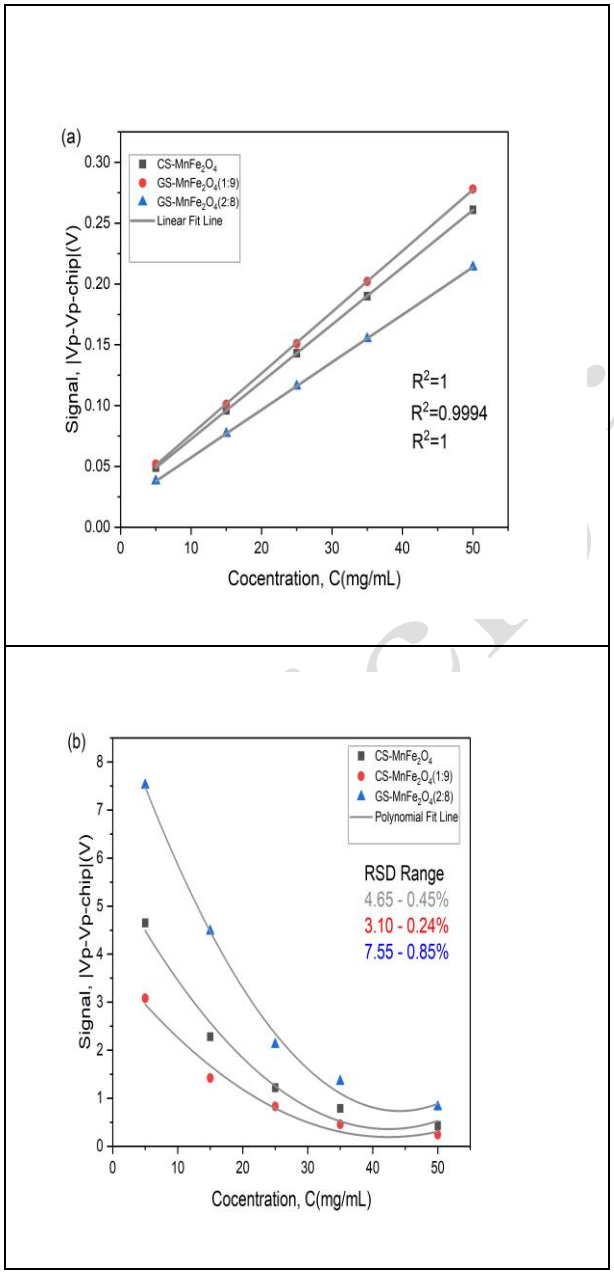

Fig. 12: (a) Sensor response *versus* concentration and (b) Replicate measurement deviation

The sensing principle is based on the variation of stray magnetic field generated by $MnFe_2O_4$ nanoparticle labels. At lower concentrations, fewer nanoparticles contribute to the magnetic signal, resulting in a smaller output voltage, whereas increasing the nanoparticle concentration strengthens the stray magnetic field and correspondingly enhances the TMR sensor response. The TMR2905 sensor effectively distinguished these concentration-dependent magnetic signals with high sensitivity. Fig. 12(b) presents relative standard deviation (RSD) values obtained for CS-$MnFe_2O_4$ and GS-$MnFe_2O_4$. An RSD of output voltage was determined by Eq. (7) (Shanavash *et al.* 2026).

$$RSD = \frac{\sqrt{\frac{\sum_{k-1}^{n}(V_x-\bar{V})^2}{n-1}}}{\bar{V}\times 100}\% \quad \ldots (7),$$

where n and V_x denote total number of measurements and measured output voltage. The calculated RSD were 4.65–0.45% for CS- $MnFe_2O_4$, 3.10–0.24% for GS-$MnFe_2O_4$(1:9), and 7.55–0.85% for GS-$MnFe_2O_4$ (2:8), with the GS-$MnFe_2O_4$ (2:8) sample showing the largest variation. This behavior is attributed to its lower M_s, as summarized in Table 6.

Table 6. Sensor performance comparison

Sample	M_2(emu/ g)	LoD (mg/ mL)	Particle Size (nm)	Sensitivity (mV/ (mg/ mL))	R^2
GS-$MnFe_2O_4$	61.50	1.20	9.11 ± 0.18	4.90	1.0000
CS-$MnFe_2O_4$ (1:9)	66.80	1.05	8.06 ± 0.17	4.20	0.9994
GS-$MnFe_2O_4$ (2:8)	34.20	1.30	6.94 ± 0.15	4.00	1.0000

The reduced magnetic response arises from the higher CM extract content, which increases the proportion of non-magnetic phytochemical residues and decreases the effective magnetic content of the nanoparticles. Consequently, fewer magnetically active particles contribute to the sensor response at low concentrations, making the measured signal more susceptible to variations in nanoparticle deposition. Although the GS- $MnFe_2O_4$ (2:8) sample exhibited comparatively higher RSD values, the repeatability remained acceptable for TMR biosensing. Furthermore, the RSD decreased progressively with increasing nanoparticle concentration, demonstrating improved measurement precision at higher magnetic label loadings.

To examine relationship among the particle size, practical detection limit (xLoD), and magnetic moment, CS-$MnFe_2O_4$ was selected as the reference sample because it exhibited a bias-field magnetization of 7.20 emu/g at 4 Oe. For the measured detection limit (xLoD = 1.20 mg/mL), assuming a deposited volume of 2 µL, number of detectable nanoparticles was calculated

as (11.4 $\times 10^{11}$), which was approximated to (9 $\times 10^{11}$) particles. The corresponding total magnetic moment was therefore estimated as (1.68 $\times 10^{-5}$) emu.

Fig. 13 shows that the green-synthesized $MnFe_2O_4$ samples exhibited only a slight increase in xLoD (1.20–1.30 mg/mL), whereas total magnetic moment decreased markedly from (1.68 $\times 10^{-5}$) to (0.92$\times 10^{-5}$) emu with increasing CM extract content. This trend indicates that higher CM substitution reduced magnetic performance of the $MnFe_2O_4$ because greater amount of surface-bound phytochemicals lowered the effective magnetic contribution. Consequently, the overall magnetic response and TMR sensing efficiency gradually decreased. However, the increase in xLoD remained relatively small despite the reduction in magnetic moment. This behavior suggests that, in addition to modifying the magnetic properties, the CM extract acted as a natural capping and stabilizing agent that improved nanoparticle dispersion and suppressed severe agglomeration. The enhanced colloidal stability partially compensated for the loss in magnetic response, allowing the TMR sensor to maintain satisfactory detection performance even at higher CM extract contents. Different magnetic attributes of $MnFe_2O_4$ are shown in Table 7.

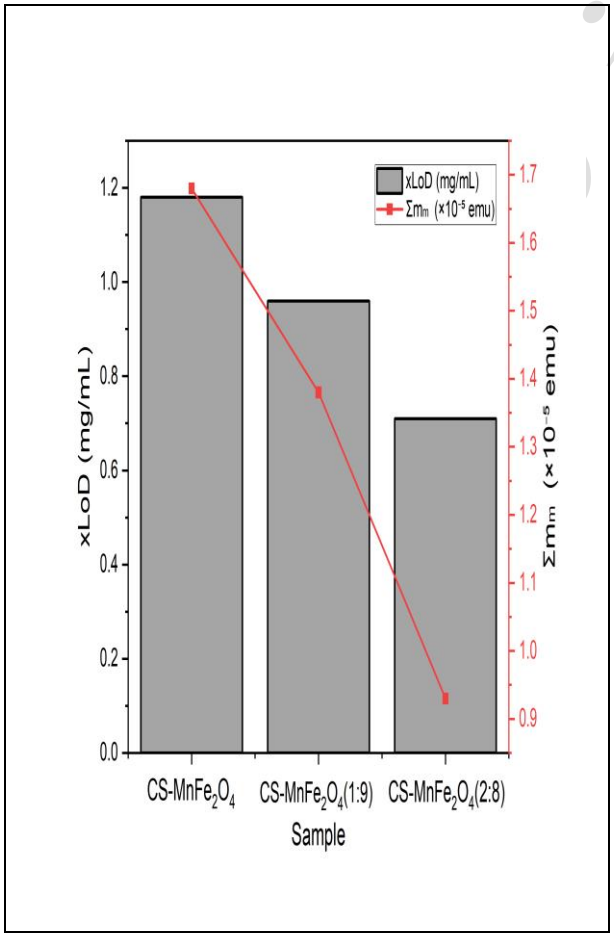

Fig. 13: Correlation between xLoD and Σmm

Table 7. Magnetic attributes of $MnFe_2O_4$

Sample	CS-$MnFe_2O_4$	GS-$MnFe_2O_4$(1:9)	GS-$MnFe_2O_4$ (2:
$xLoD$ (mg /mL)	1.20	1.05	1.30
n_{grom} ($\times 10^{17}$ /g)	4.83	5.21	8.22
M (emu/g)	7.20	6.65	3.45
m_m ($\times 10^{-17}$)	1.49	1.28	0.42
N ($\times 10^{11}$)	11.40	10.00	11.67
N_{actual} ($\times 10^{11}$)	11	10	12
Σm_m($\times 10^{-5}$ei	1.68	1.38	0.92

Fig. 14 illustrates the operating principle of the TMR2905 sensing system. Initially, as shown in Fig. 14(a), a 2 µL aliquot of the ethanol-dispersed $MnFe_2O_4$ nanoparticle suspension was deposited onto the active sensing region and allowed to dry completely. Magnetic bias field of 4 Oe was applied along easy axis of TMR sensor. The sensing response originates from the magnetic tunnel junction, where the relative orientation of the pinned and free magnetic layers determines the electrical resistance. Without an external magnetic field, the two layers remain predominantly antiparallel, producing a high-resistance state. Under the applied bias field, the free layer rotates toward parallel alignment with the pinned layer, decreasing the junction resistance and changing the output voltage.

As illustrated in Fig. 14(b), the deposited $MnFe_2O_4$ nanoparticles generate localized stray magnetic fields that modify the effective magnetic field experienced by the TMR sensor. The resulting field perturbation changes the resistance of the magnetic tunnel junction, leading to a measurable variation in output voltage. Increasing the nanoparticle concentration strengthens the stray magnetic field and correspondingly increases the sensor response. The measured resistance values under different magnetic field conditions confirmed the concentration-dependent sensing behavior $R_{max} > R_c > R_b > R_a$.

Among the investigated samples, GS-$MnFe_2O_4$ (1:9) exhibited the highest saturation magnetization (66.80 emu/g), greatest sensor sensitivity 4.20 mV/(mg/mL), demonstrating superior performance among the synthesized magnetic labels. These results confirm that *Cucurbita moschata*-assisted green synthesis can produce $MnFe_2O_4$ nanoparticles with excellent magnetic and sensing characteristics while providing the environmental benefits of a plant-mediated synthesis route. Nevertheless, further optimization of

particle size and magnetic properties could further improve the overall TMR biosensing performance.

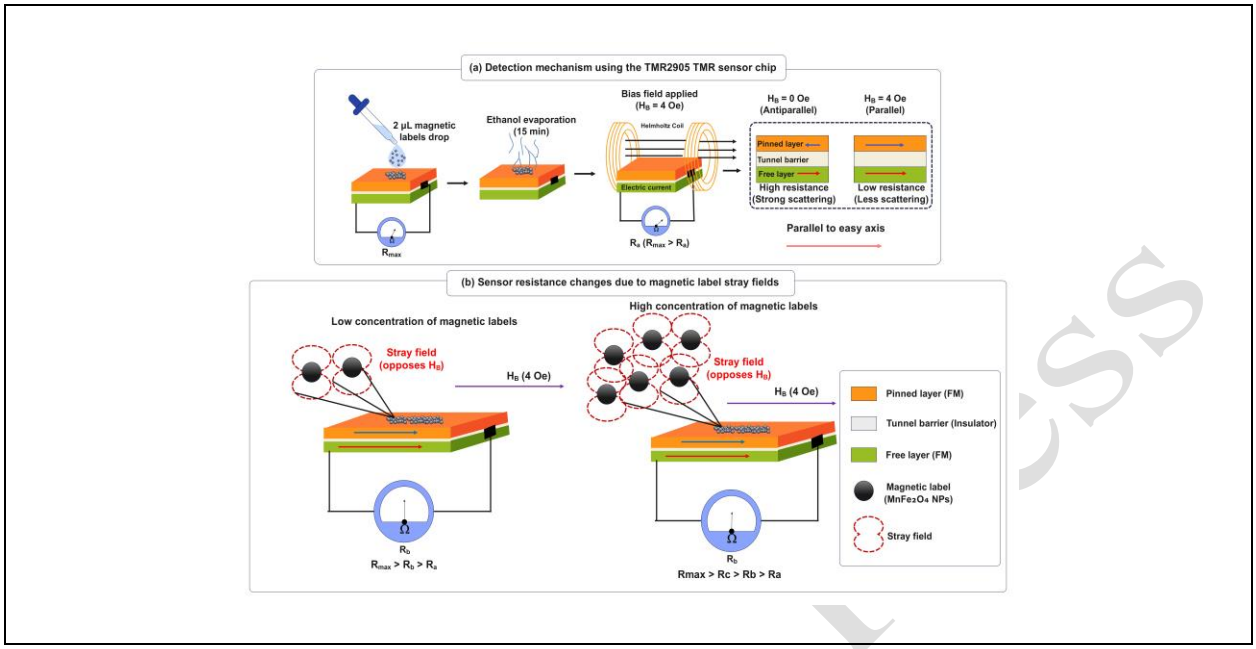

Fig. 14: (a) TMR2905 sensing mechanism and (b) Resistance variation under magnetic fields

4. CONCLUSION

An environmentally benign route for synthesizing $MnFe_2O_4$ nanoparticles using *Cucurbita moschata* leaf extract was successfully demonstrated, and the influence of different CM:NH_4OH ratios (1:9, 2:8, 3:7, and 4:6) on the structural, magnetic, and TMR sensing characteristics was systematically evaluated. Among the synthesized samples, GS-$MnFe_2O_4$ (1:9) delivered the highest saturation magnetization (66.80 emu/g) and best TMR sensor sensitivity (4.20 mV/(mg/mL)), indicating most effective combination of green synthesis and magnetic performance. Increasing the CM extract content beyond this ratio gradually reduced crystallinity and magnetic behavior, demonstrating that CM leaf extract functions most effectively as a green-assisted stabilizing and reducing agent rather than a complete replacement for NH_4OH. For applications prioritizing environmental sustainability, the GS- $MnFe_2O_4$ (2:8) sample provides a practical alternative by maintaining acceptable magnetic performance (M_s = 34.20) and sensor sensitivity (4.00 mV/(mg/mL)) increasing contribution of the plant-derived reagent. Structural and magnetic analyses verified the successful formation of soft-ferromagnetic $MnFe_2O_4$ nanoparticles with low coercivity (Hc < 132 Oe). The developed TMR2905 sensing platform exhibited excellent analytical performance, including high sensitivity (4.00–4.20 mV/(mg/mL)), strong linearity (R^2 = 0.98–0.99), low limits of detection (1.05–1.30 mg/mL), and a rapid response with 30 s. Integration of green-synthesized $MnFe_2O_4$ nanoparticles with the TMR2905 sensor provides an efficient, sustainable, and tunable magnetic biosensing platform. The GS-$MnFe_2O_4$ (1:9) formulation is recommended where maximum sensing performance is required, whereas the GS-$MnFe_2O_4$ (2:8) formulation offers a more environmentally sustainable option without a substantial loss in sensing capability.

FUNDING

This research received no specific grant from any funding agency in the public, commercial, or not-for-profit sectors.

CONFLICTS OF INTEREST

The authors declare that there is no conflict of interest.

REFERENCES

Alghamdi, W., Mayakannan, S., Sivasankar, G. A., Singh, J., Ravi, N. B. and Venkata, K. R. C., Turbulence Modeling Through Deep Learning: An In-Depth Study of Wasserstein GANs, *2023 4th Int. Conf. Smart Electron. Commun.*, 793–797(2023). https://doi.org/10.1109/ICOSEC58147.2023.10275878

Al-Sawaff, Z. H., Rashid, Z. M., Al-Okby, M. F. R. and Kandemirli, F., A microcontroller based microfluidic biochip for calcium percentage detection in blood, *Indones. J. Electric. Eng. Comp. Sci.*, 26(1), 135–142(2022). https://doi.org/10.11591/ijeecs.v26.i1.pp135-142

Amara, S., Aljedaibi, A., Alrashoudi, A., Ben Mbarek, S., Khan, D. and Massoud, Y., High-performance MTJ-based sensors for monitoring of atmospheric pollution, *AIP Adv.*, 13(3), 035329(2023). https://doi.org/10.1063/9.0000496

Ardiyanti, H., Mabarroh, N., Wibowo, N. A., Istiqomah, N. I., Tumbelaka, R. M., Darmawan, M. Y., Zurnansyah, Z., Prabowo, Y. D., Absor, M. A. U. and Suharyadi, E., Facile and Fast Assay of Biomolecule Using ICs-Based Giant Magnetoresistance Chip Sensor with Green-Synthesized Manganese ferrite Nanotag, *Sensing Imaging*, 26(1), 75(2025). https://doi.org/10.1007/s11220-025-00597-3

Chandrasekar, M., Subash, M., Logambal, S., Udhayakumar, G., Uthrakumar, R., Inmozhi, C., Al-Onazi, W. A., Al-Mohaimeed, A. M., Chen, T.-W. and Kanimozhi, K., Synthesis and characterization studies of pure and Ni doped CuO nanoparticles by hydrothermal method, *J. King Saud Univers. Sci.*, 34(3), 101831(2022). https://doi.org/10.1016/j.jksus.2022.101831

Chandrasekar, M., Subash, M., Perumal, V., Aravindan, S., Uthrakumar, R., Inmozhi, C., Babujanarthanam, R. and Kaviyarasu, K. Specific charge separation of Cd doped TiO_2 photocatalysts for energy applications. *Materials Science for Energy Technologies. 6*, 472–483. (2023). https://doi.org/10.1016/j.mset.2023.04.010

Da Silva, F. J., Oliveira, L. C. and Lima, A. M. N., An Automated Platform for Surface Plasmon Resonance-Based Sensors, *IEEE Trans. Instru. Measure.*, 70, 1-7 (2021). https://doi.org/10.1109/TIM.2021.3084315

Dhillon, G., Kumar, N., Chitkara, M. and Sandhu, I. S., Effect of A-site substitution and calcination temperature in Fe_3O_4 spinel ferrites, *J. Mater. Sci. Mater. Electron.*, 31(21), 18903–18912(2020). https://doi.org/10.1007/s10854-020-04427-y

Garcia, S., Mabarroh, N., Darmawan, M. Y., Wibowo, N. A., Ardiyanti, H., Tumbelaka, R. M., Istiqomah, N. I. and Suharyadi, E., Two spin-valve GMR thin films on half wheatstone bridge circuit for detecting green-synthesized Fe_3O_4@Ag nanoparticles-labeled biomolecule, *Materialia*, 32, 101930(2023). https://doi.org/10.1016/j.mtla.2023.101930

Gayathri, S., Swetha, A., Kumar, A., Muniyasamy, M. K., Premkumar, S. and Pavithra, G., Biogenic SiO_2 Nanoparticles Derived from Diatomaceous Biosludge for Sub-ambient Radiative Cooling Geopolymer Coatings, *J. Environ. Nanotechnol*,. 15(1), 643–657 (2026). https://doi.org/10.13074/jent.2026.03.2612083

Ghemes, C., Dragos-Pinzaru, O.-G., Tibu, M., Lostun, M., Lupu, N. and Chiriac, H., Tunnel Magnetoresistance-Based Sensor for Biomedical Application: Proof-of-Concept, *Coat*,. 13(2), 227(2023). https://doi.org/10.3390/coatings13020227

Jin, Z., Koo, T. M., Kim, M. S., Al-Mahdawi, M., Oogane, M., Ando, Y. and Kim, Y. K., Highly-sensitive magnetic sensor for detecting magnetic nanoparticles based on magnetic tunnel junctions at a low static field, *AIP Adv.*, 11(1), 015046(2021). https://doi.org/10.1063/9.0000189

Kanthiah, A., Manimaran, E. I. and Vignesan, N., A Study on the Magnetic Properties of Electrodeposited Cobalt-based Monolayer and Multilayer Alloys for Magnetic Sensor Application, *J. Environ. Nanotechnol.*, 15(1), 232–242 (2026). https://doi.org/10.13074/jent.2026.03.2541861

Lambertini, E., Penolazzi, L., Pellielo, G., Pipino, C., Pandolfi, A., Fiorito, S., Epifano, F., Genovese, S. and Piva, R., Pro-osteogenic properties of violina pumpkin (Cucurbita moschata) leaf extracts: Data from in vitro human primary cell cultures, *Nutri.*, 13(8), 2633(2021). https://doi.org/10.3390/nu13082633

Li, Y., Chen, X., Zhang, Z., Xu, X. and Zhao, J., Design of automatic high-precision biochip spotting head based on STM32, *Electric. Measure. Instrument.*, 57(13), 144–148 (2020). https://doi.org/10.19753/j.issn1001-1390.2020.13.023

Montoya-Leyva, G. E., Berman-Mendoza, D., Ramos-Carrazco, A., López-Delgado, R., Rangel, R., Hernández-Abril, P. A. and Higuera-Valenzuela, H. J., Optical Biosensor for Glucose Detection Based on the Green Synthesis of Silicon Nanoparticles using *Ocimum basilicum purpurascens* Extract, *Silicon*, 17(10), 2329–2345 (2025). https://doi.org/10.1007/s12633-025-03351-2

Moron-Fernandez, C., Verdu-Vazquez, A., Gil-Lopez, T. and Moron-Barrios, A. Microscope Stand for the Measurement and Characterization of Amorphous Ferromagnetic Materials, *IEEE Trans. Instrument. Measure*,. 70, 1-7(2021). https://doi.org/10.1109/TIM.2021.3082323

Nawale, S. P., Dube, P. B., Wani, S. M., Keche, A. P. and Jadhav, K. M., Gd-doped Ni-Zn spinel ferrite nanoparticles via piper nigrum-mediated synthesis: Structural, optical, magnetic, and antibacterial properties, *Solid State Commun.*, 416, 116489(2026). https://doi.org/10.1016/j.ssc.2026.116489

Nemčeková, K., Dudoňová, P., Holka, T., Balážová, S., Hornychová, M., Szebellaiová, V., Naumowicz, M., Gemeiner, P., Mackuľak, T., Gál, M. and Svitková, V., Silver Nanoparticles for Biosensing and Drug Delivery: A Mechanical Study on DNA Interaction, *Biosens.*, 15(5), 331(2025). https://doi.org/10.3390/bios15050331

Parimalagandhi, K., Rajendran, S., Esakkiammal, M., Sudha, P. and Simi, A., Smart Nanosensors for Assessing Nanoparticle Interactions in Crops: A Review, *J. Environ. Nanotechnol.*, 14(4), 185–191 (2025). https://doi.org/10.13074/jent.2025.12.2531753

Pekdemir, S., Özen Öner, E., Pekdemir, M. E., Dalkılıç, S. and Kadıoğlu Dalkılıç, L., An Investigation into the Influence of C. moschata Leaves Extract on Physicochemical and Biological Properties of Biodegradable PCL/PLA Blend Film, *J. Polym. Environ.*, 30(9), 3645–3655 (2022). https://doi.org/10.1007/s10924-022-02460-y

Pilati, V., Salvador, M., Fraile, L. B., Marqués-Fernández, J. L., Gomes da Silva, F., Fadel, M., López Antón, R., Morales, M. D. P., Martinez-García, J. C. and Rivas, M., Mn-ferrite nanoparticles as promising magnetic tags for radiofrequency inductive detection and quantification in lateral flow assays, *Nanoscale Adv.*, 6(16), 4247–4258(2024). https://doi.org/10.1039/d4na00445k

Rizki, M., Swastika, P. E., Ardiyanti, H., Shifa, L., Ajrina, H., Istiqomah, N. I., Mahardhika, L. J., Prabowo, Y. D., Kurniawan, C., Angel, J., Risdiana, R., Djuhana, D. and Suharyadi, E., Rapid quantitative assay of eco-friendly SiO_2-functionalized Fe_3O_4 nanoparticles using GMR and TMR-based sensor, *J. Sci. Adv. Mater. Dev.*, 11(2), 101171(2026). https://doi.org/10.1016/j.jsamd.2026.101171

Salama, R., Alghamdi, W., Alsalmi, H. M., Mayakannan, S., Taqui, S. N. and Deepalakshmi, R., Evolution of Service-Oriented Computing: Integrating Quantum Techniques for Integer Factorization, *2024 IEEE 9th Int. Conf. Converge. Technol.*, 1-6(2024). https://doi.org/10.1109/I2CT61223.2024.10543362

Sayad, A., Uddin, S. M., Yao, S., Wilson, H., Chan, J., Zhao, H., Donnan, G., Davis, S., Skafidas, E., Yan, B. and Kwan, P., A magnetoimpedance biosensor microfluidic platform for detection of glial fibrillary acidic protein in blood for acute stroke classification, *Biosens. Bioelectron.*, 211, 114410(2022). https://doi.org/10.1016/j.bios.2022.114410

Shanavash, A., Sri, T. S., Mayakannan, S., Shanmugam, S. K., Chandankhede, P. H. and Sivakumar, B. G., Development of a carbon–perovskite self-powered IoT sensor node with dual-mode sensing, *Interact.*, 247(1), 175(2026). https://doi.org/10.1007/s10751-026-02516-8

Swastika, P. E., Ardiyanti, H., Darmawan, M. Y., Mahardika, L. J., Istiqomah, N. I., Wibowo, N. A. and Suharyadi, E., Enhanced detection of bovine serum albumin using single- and double-chip configuration of tunneling magnetoresistance–based biosensor with green-synthesized manganese ferrite/Ag nanotag, *Microchimica Acta.*, 192(3), 143(2025). https://doi.org/10.1007/s00604-025-07005-3

Swastika, P. E., Ardiyanti, H., Puspitarum, D. L., Istiqomah, N. I., Wibowo, N. A. and Suharyadi, E., Commercial chip-based tunneling magnetoresistance sensor for green-synthesized magnetic nanoparticles assay, *Sens. Int.*, 5, 100288 (2024). https://doi.org/10.1016/j.sintl.2024.100288

Tabrani, R. A. H., Antarnusa, G. and Firdaus, F., Facile synthesis of Fe_3O_4 via co-precipitation method: The role of Moringa oleifera in substituting chemical reducing agents, *Next Mater.*, 8, 100927(2025). https://doi.org/10.1016/j.nxmate.2025.100927

Wang, M., Tao, X., Peng, L. and Ye, C., Imaging of Magnetic Nanoparticles Using Small TMR Sensor with an Excitation-Compensation Scheme, *IEEE Sens. J.*, 20(19), 11082–11089(2020). https://doi.org/10.1109/JSEN.2020.2996741

Wibowo, N. A., Hariyanto, D. M., Darmawan, M. Y., Ardiyanti, H., Istiqomah, N. I., Nakamura, K. and Suharyadi, E., Development of a Reliable Assay of Eco-friendly Fe_3O_4@Ag Nanocomposite-Based Giant Magnetoresistance Sensor, *J. Electrochem. Society*, 171(11), 117501(2024). https://doi.org/10.1149/1945-7111/ad8a8f

Yadav, N., Singh, A. and Kaushik, M., Synthesis and characterization of hydrothermally synthesized superparamagnetic APTS–$ZnFe_2O_4$ nanoparticles: DNA binding studies for exploring biomedical applications, *J. Electrochem. Soc.*, 74(4), 1177–1188 (2020). https://doi.org/10.1007/s11696-019-00953-0

Yao, Y., Qiu, D., Liu, H., Yang, Z., Liu, X., Yang, Y. and Dong, C., A Reliable and Secure Mobile Cyber-Physical Digital Microfluidic Biochip for Intelligent Healthcare, *IEEE Access*, 11, 137990–137998 (2023). https://doi.org/10.1109/ACCESS.2023.3339386